The Journal of Immunology

Subtle CXCR3-Dependent Chemotaxis of CTLs within Infected Tissue Allows Efficient Target Localization

Silvia Ariotti, Joost B. Beltman, Rianne Borsje, Mirjam E. Hoekstra, William P. Halford, John B. A. G. Haanen, Rob J. de Boer and Ton N. M. Schumacher

Supplementary Material	http://www.jimmunol.org/content/suppl/2015/10/31/jimmunol.1500853.DCSupplemental.html
References	This article **cites 33 articles**, 14 of which you can access for free at: http://www.jimmunol.org/content/195/11/5285.full#ref-list-1
Subscriptions	Information about subscribing to *The Journal of Immunology* is online at: http://jimmunol.org/subscriptions
Permissions	Submit copyright permission requests at: http://www.aai.org/ji/copyright.html
Email Alerts	Receive free email-alerts when new articles cite this article. Sign up at: http://jimmunol.org/cgi/alerts/etoc

Subtle CXCR3-Dependent Chemotaxis of CTLs within Infected Tissue Allows Efficient Target Localization

Silvia Ariotti,*,[1] Joost B. Beltman,*,†,‡,[1] Rianne Borsje,* Mirjam E. Hoekstra,*
William P. Halford,§ John B. A. G. Haanen,* Rob J. de Boer,† and Ton N. M. Schumacher*

It is well established how effector T cells exit the vasculature to enter the peripheral tissues in which an infection is ongoing. However, less is known regarding how CTLs migrate toward infected cells after entry into peripheral organs. Recently, it was shown that the chemokine receptor CXCR3 on T cells has an important role in their ability to localize infected cells and to control vaccinia virus infection. However, the search strategy of T cells for virus-infected targets has not been investigated in detail and could involve chemotaxis toward infected cells, chemokinesis (i.e., increased motility) combined with CTL arrest when targets are detected, or both. In this study, we describe and analyze the migration of CTLs within HSV-1–infected epidermis in vivo. We demonstrate that activated T cells display a subtle distance-dependent chemotaxis toward clusters of infected cells and confirm that this is mediated by CXCR3 and its ligands. Although the chemotactic migration is weak, computer simulations based on short-term experimental data, combined with subsequent long-term imaging indicate that this behavior is crucial for efficient target localization and T cell accumulation at effector sites. Thus, chemotactic migration of effector T cells within peripheral tissue forms an important factor in the speed with which T cells are able to arrive at sites of infection. *The Journal of Immunology*, 2015, 195: 5285–5295.

A striking characteristic of the cells of the immune system is their ability to travel throughout the organism to guard peripheral tissues and to prevent the spread of infection. First, APCs acquire Ag within peripheral tissues and travel to draining lymph nodes to present the collected Ags to naive T cells (1, 2). Ag-specific T cells that are activated by APC encounter then initiate expression of effector molecules, such as perforin and granzymes, and enter the blood stream via the efferent lymph. Extravasation of such activated T cells preferentially takes place at sites of infection, through regulation of adhesive interactions with the vascular endothelium (3). Several studies have examined the interaction between CTLs and target cells at sites of infection (4–6). In another recent study by Hickman et al. (7), it was shown that expression of the chemokine receptor CXCR3 on T cells assists in the localization, killing, and control of vaccinia virus (VV) infection. However, the exact search strategy by which CXCR3 expres-

sion helps T cells to detect virus-infected targets has not yet been elucidated. On the one hand, this could be obtained by chemokinesis (i.e., a general increase of cellular motility that occurs upon encounter of specific chemokine ligands). For example, such chemokinetic effects occur for CXCR7-expressing T cells within lymph nodes (8). On the other hand, CTLs could migrate directionally toward sites of infection by CXCR3-mediated chemotaxis, a process that should also reduce the time with which established sites are reached. A large number of studies have described the migration patterns of T and B lymphocytes within lymph nodes (reviewed in Ref. 9), and evidence for such directed migration has been obtained in several of them (10–14). Within peripheral tissues (i.e., subsequent to extravasation), it was recently proposed that the observed CD8+ T cell clustering around malaria-infected hepatocytes is consistent with directed migration (15), but direct evidence for chemotaxis was not obtained. On the contrary, other recent literature suggests that CTLs in pancreas and brain adopt random search strategies (16, 17).

In this study, we develop and use a skin infection intravital imaging setup in which the epidermis of recipient animals is infected with HSV-1. Imaging of virus-specific and bystander CTLs within the epidermis of infected mice indicates that both T cell populations migrate through the epidermis without any directional preference that can be appreciated by direct observation. Importantly though, quantitative analysis of the data and subsequent computer simulations based on these experimental data demonstrate that there is a small preference to migrate toward sites of infection. As expected, and on the basis of the recent findings by Hickman et al. (7), this preference depends on CXCR3 expression on T cells and can be influenced by disturbance of CXCR3 ligands. Furthermore, this preference translates to a marked increase in the efficiency with which effector T cells accumulate at the sites of infection. Thus, our results reveal how subtle chemotaxis of cytotoxic T cells within the periphery allows the efficient localization of clusters of pathogen-infected cells during an antiviral immune response.

*Division of Immunology, Netherlands Cancer Institute, 1066 CX Amsterdam, the Netherlands; †Theoretical Biology and Bioinformatics, Utrecht University, 3584 CH Utrecht, the Netherlands; ‡Division of Toxicology, Leiden Academic Centre for Drug Research, Leiden University, 2333 CC Leiden, the Netherlands; and §Department of Medical Microbiology, Immunology and Cell Biology, Southern Illinois University School of Medicine, Springfield, IL 62794

[1]S.A. and J.B.B. contributed equally to this work.

ORCIDs: 0000-0003-4434-9813 (M.E.H.); 0000-0001-5884-7704 (J.B.A.G.H.); 0000-0002-2130-691X (R.J.d.B.).

Address correspondence and reprint requests to Prof. Ton N.M. Schumacher, Netherlands Cancer Institute, Plesmanlaan 121, Amsterdam, 1066 CX, the Netherlands. E-mail address: t.schumacher@nki.nl

The online version of this article contains supplemental material.

Abbreviations used in this article: 2D, two-dimensional; 3D, three-dimensional; NKI, Netherlands Cancer Institute; VV, vaccinia virus.

Materials and Methods

Mice

C57BL/6, C57BL/6 actin-GFP, and C57BL/6 OTI TCR transgenic mice were obtained from Charles River Laboratories and housed in the animal facility of the Netherlands Cancer Institute (NKI). C57BL/6 gBT TCR transgenic mice (18) were a gift from Dr. F. Carbone (University of Melbourne, Australia). All animal experiments were approved by the Experimental Animal Committee of the NKI, in accordance with national guidelines.

Reagents

Abs against MHC II, CD4, CD11b, CD11c, Ter-119, CD49b, CD45R, Gr-1, and CD8 were obtained from BD Biosciences. MHC-tetramers loaded with SIINFEKL (Ova$_{257-264}$) or SSIEFARL (gB$_{498-505}$) peptides were produced by UV-induced ligand exchange (19) and labeled with PE or APC (Invitrogen).

DNA vaccines were generated by the introduction of the indicated fusion genes in pVAX. Tetanus Toxin Fragment C (TTFC)-Ova and TTFC-gB DNA sequences were designed for optimized codon usage, and encoded domain I of TTFC and the indicated T cell epitope, separated by a GVQI peptide linker. HSV$_{TOM}$ and HSV$_{TOM-OVA}$ viruses were constructed by the insertion of a CMV immediate-early promoter-tomato (or tomato-Ova$_{257-264}$) gene cassette into the intergenic region between the UL26 and UL27 genes of the HSV-1 strain KOS, as described previously (20).

Flow cytometry

For the measurement of T cell responses, 25 μl of peripheral blood was collected in heparin-coated vials (Microvette; Omnilabo) at the indicated days after transfer. After removal of erythrocytes by NH$_4$Cl treatment, cells were stained with the indicated Abs and analyzed by flow cytometry. Dead cells were excluded by DAPI staining. Cell sorting was performed on a FACSAria cell sorter using FACSDiva software (version 5.0.1; both from BD), or a MoFlo high-speed sorter using Summit software (version 3.1; both from Beckman Coulter). Analyses were performed on a CyAn$_{ADP}$ using Summit software (version 4.3; both from Beckman Coulter).

Adoptive transfer and intradermal DNA vaccination

Spleens from GFP-gBT or GFP-OTI mice were isolated and homogenized by mincing through cell strainers (BD Falcon). After RBC lysis, CD8$^+$ T cells were isolated using MHC II$^+$, CD4$^+$, CD11b$^+$, CD11c$^+$, Ter-119$^+$, CD49b$^+$, CD45R$^+$, and Gr-1$^+$ staining as exclusion criteria. C57BL/6 mice were injected i.v. with 2.0 × 10^5 sorted naive CD8$^+$ T cells. Intradermal DNA vaccination with either TTFC-Ova or TTFC-gB was performed on the shaved hind leg of anesthetized mice, as described previously (21). A droplet of 30 μg DNA in 15 μl PBS was applied onto the skin and injected using a sterile disposable 11-needle bar mounted on a rotary tattoo device. Needle depth was adjusted to 0.5 mm, and the needle bar oscillated at 100 Hz for a 60-second tattoo.

HSV-1 infection, quantitative PCR, and immunohistochemistry

Indicated HSV strains were grown in Vero cells as described previously (22), and intraepithelial HSV-1 infection was completed on the shaved flank of anesthetized mice. A droplet of 20 μl virus-infected Vero cell supernatant containing ~2.5 × 10^5 PFU was applied onto the skin and introduced as described for intradermal vaccination, but with needle depth adjusted to 0.05 mm, for a 20-second tattoo. At the indicated time points postinfection, mice were sacrificed by cervical dislocation; the skin of the infected flank was collected and divided into two separate specimens that were further treated independently. HSV titers (Artus HSV-1/2 TM PCR Kit; Qiagen) were analyzed in triplicate on each half sample, according to protocol. HSV infection was visualized by incubation with rabbit polyclonal anti HSV Ab (Thermo Scientific), followed by PowerVision Poly-HRP-Goat anti Rabbit staining (ImmunoLogic) and DAB reaction (Dako Cytomation), according to protocol.

Confocal microscopy and image analysis

Twenty-four hours after HSV infection, mice were anesthetized using a mixture of air and isoflurane (Baxter) and placed in a custom-built chamber with the infected flank gently placed against a coverslip at the bottom side of the chamber. Images were acquired using an inverted Leica TCS SP2 confocal scanning microscope (Leica Microsystem) equipped with Diode and Argon lasers and enclosed in a custom-built environmental chamber that was maintained at 37°C using heated air. Images were acquired using a 20×/0.7 NA dry objective unless indicated otherwise. GFP was excited at 488 nm wavelength and tandem dimer tomato at 561 nm. Typical voxel dimensions were 0.9–2.0 μm laterally × 1.5–2.5 μm axially. Three-dimensional stacks (typical size: ~500 × ~500 × ~30 μm) were captured every minute for a period of up to 2 h. Raw imaging data were processed with Imaris (Bitplane). Imaris Spots module was used to track objects and to calculate cell coordinates (mean positions) over time (representative track in Supplemental Video 4). The resulting tracks were manually checked for correctness, and any track part that was uncertain from the viewpoint of a human observer was excluded. Although this approach results in the splitting of long tracks into short ones, it does not influence the predominantly step-based approaches that are used for subsequent analysis (23).

Cell migration analysis

The cell coordinate data that resulted from tracking were corrected for artifacts as described previously (23). In brief, presumed static autofluorescent hair follicles or the infection region itself were used for tissue drift correction, and accuracy of drift correction was checked by visual inspection of videos. Movement steps close to the borders of the image volume were discarded from analysis, because they would appear to move parallel to those borders because of tracking errors (note that an advantage of two-dimensional [2D] over three-dimensional [3D] analyses is that a much smaller number of movement steps need to be discarded for this reason). Finally, imprecision in the axial resolution was either left uncorrected (data not shown) or corrected by multiplying the mean axial speed of cells by a factor (varying between 1.2 and 2.95 depending on the experiment) that made it approximately equal to their mean lateral speed. Because of the flat structure of the epidermis, it is possible that axial speeds are in fact much slower than lateral speeds. Omitting the axial speed correction would entail that the lateral movements are much more important than the axial movements in determining arrival at microlesions (i.e., that migration is effectively 2D). Importantly though, the observed directional preference of CTLs toward infected microlesions (see below) was observed both with and without the correction for axial speed.

After correction for these artifacts, the following parameters were calculated from the cell coordinates: 1) cell speeds (during individual movement steps), 2) turning angles (i.e., the angle between subsequent movement steps of a cell or between longer time intervals for a single cell), 3) distances to infection (i.e., distance between the center of mass of a cell and the location of the most nearby voxel that was assigned to the infection when using a segmentation threshold following application of a Gaussian filter to smoothen the images), 4) angles to infection (i.e., the angle between the direction of migration of a cell and the direction toward the nearest voxel assigned to the infection), and 5) displacement rates toward infection (calculated from the projection of a movement step onto the vector that represents the shortest route toward the nearest voxel assigned to the infection). Note that all the studied migration parameters are averages measured over 1-min time frames.

Model of cell migration

Cell motion was modeled by describing it as a series of discrete steps in space. Simulations were performed in two or three dimensions, and either as directed or random simulations. For directed simulations, the experimental distributions of speed, angle to infection, and turning angle were used after merging the data from four to five experiments that were performed under the same conditions. Measured pairs of speed and angle to infection were maintained during directional simulations. In random simulations, the angles to infection were chosen from a distribution as expected for random migration, i.e., a uniform distribution in 2D and a sine distribution in 3D. The distributions of speed and angle to infection were sorted according to the distance to infection at which the measurement was taken. Subsequently, the speed/angle-to-infection pairs were binned into distance categories containing 100 measurements each. Each of the distance bins would also be accompanied by a turning angle distribution (containing all the turning angles experimentally measured in that distance bin). In the simulations, a microlesion was modeled as a circle (in 2D) or sphere (in 3D) with radius r. Each in silico cell was initialized at the indicated distance from the simulated infection, and the initial movement step of the cell was chosen at random from the 100 speed/angle-to-infection combinations in the appropriate distance category. In 2D simulations, each combination is associated with two possible movement steps, and one of them would be chosen at random. In 3D simulations, the possible movement steps for each combination can be described by a circle in 3D space, and a random position on that circle was chosen. The cell was then moved to the new position defined by the chosen step. Subsequent movement steps were again chosen from the allowed speed/angle-to-infection pairs. However, if the movement steps were to be chosen randomly from the pairs, a turning angle distribution without any persistence would ensue. In
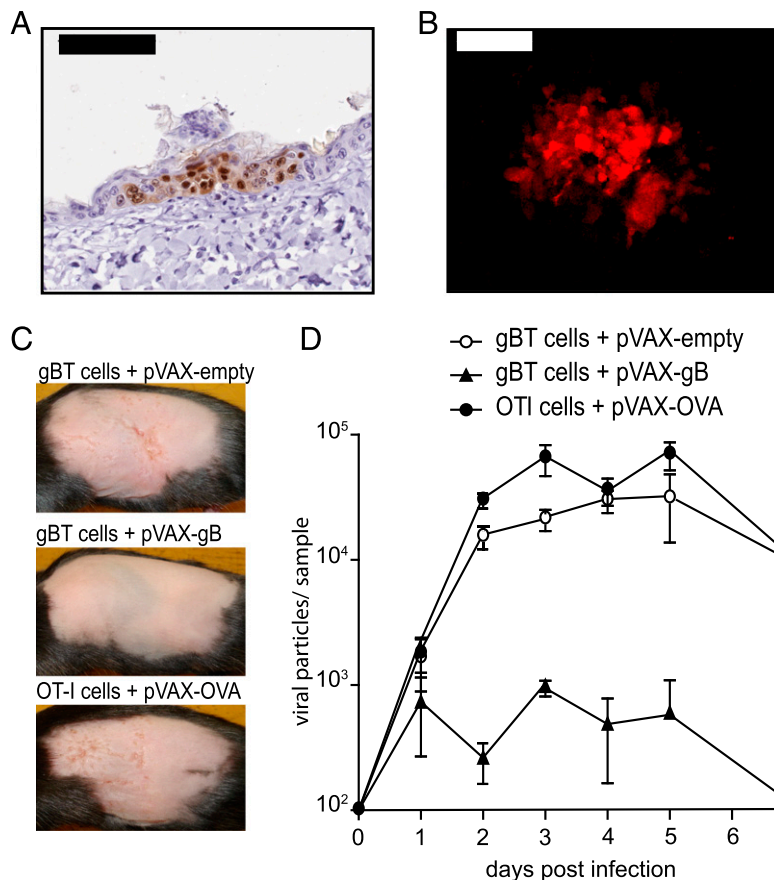
FIGURE 1. Characterization of intraepithelial HSV-1 infection. (**A**) Transverse section of paraffin-embedded skin stained with anti-HSV Ab (brown), 24 h after intra-epithelial infection with HSV$_{TOM}$. Scale bar, 100 µm. (**B**) Confocal (top view) image of an HSV-1 infected area (red), 24 h after intraepithelial infection with HSV$_{TOM}$. Scale bar, 100 µm. (**C** and **D**) Recipients of naive GFP-gBT or GFP-OTI T cells were vaccinated with DNA encoding the indicated epitope or with empty vector. Ten days later, the flank skin was intra-epithelially infected with HSV$_{TOM}$. (C) Photographs of mice in the different experimental conditions at day 7 postinfection. (D) On the indicated days postinfection, mice ($n = 3$ per group, representative of two experiments) were sacrificed, and viral titers in HSV-infected skin were determined by quantitative PCR. Data are represented as mean ± SEM.

particular, this would lead to a turning angle distribution close to a uniform distribution for 2D simulations and close to a sine distribution for 3D simulations (23). Therefore, we built in the extra restriction that a chosen movement step was accepted with a probability that would ensure a similar turning angle distribution in the simulations as in the experimental data. To achieve that, the turning angle distribution of each distance category was discretized into 18 bins of 10 degrees wide, and the proportion p_i of each turning angle bin was recorded for all distance categories (where i represents the turning angle bin number from 0 to 18). For 2D simulations, we took the proportion of the turning angle bin in which the step under consideration would fall (p_i) as the acceptance probability for that step. For 3D simulations, the proportion of each turning angle bin was first weighted by the factor $w_i = 1/\int_{\alpha=a}^{b}\sin(\alpha)d\alpha = 1/(\cos(a) - \cos(b))$, where a and b are the lower and upper limit of a turning angle bin (e.g., for the first bin $a = 0$ and $b = 10$ degrees). Next, the weighted and normalized proportion $\frac{p_i w_i}{\sum_i p_i w_i}$ was used as acceptance probability for the step. This normalized weighting of proportions ensured that speed-angle-to-infection combinations were sampled in a manner that resulted in a correct turning angle distribution. When a movement step was not accepted, another movement step would be chosen at random until one was accepted.

We performed two types of 3D simulations: one in which CTL movement was restricted at the exterior side, and one in which it was in addition restricted at the interior side. These restrictions were implemented by discarding movement steps that would result in a crossing of the interior or exterior side during the sampling of movement steps.

2D simulations of long-term (up to 12 h) T cell accumulation were performed. Infection growth was described as linear, radial growth following experimental measurements of infection sizes, and directed and random cell migration were simulated as described above. For bystander OTI cells, we considered the possibility that T cells reaching the infection from that moment could leave the simulated region (in the axial direction, i.e., by leaving the epidermis). In these simulations with leaving, T cells that had earlier reached the infection, left with probability δ at each time step.

Statistical methods

A linear mixed effects model was constructed to determine whether viral load differed between treatments over the week after inoculation. Joint Wald tests

were performed on linear and quadratic coefficients, and Bonferroni-adjusted significance level for the two-sided test was set at 0.017.

Because of persistent migration of T cells at short time intervals, subsequent movement steps are not independent. Therefore, statistics were applied to steps that were at least 10 min apart, because for skin T cells the correlation in movement direction was approximately lost after this time interval (see Fig. 2C). Two-tailed Mann–Whitney tests (using the software package R) were performed to study whether cell migration differs from a random walk, and to compare migration parameters in different conditions. Spearman's rho between distance from infection and the number of cells at that distance was calculated to study whether spatial distributions exhibited a consistent decline with distance from infection, as expected for chemoattraction toward foci of infection. A p value <0.05 was considered significant.

Results

Imaging effector T cell migration in the skin

To detect HSV-1–infected cells within an otherwise normal tissue in vivo, we generated HSV-1 recombinant viruses that either express the tandem dimer tomato fluorescent protein alone (HSV$_{TOM}$), or in combination with the Ova$_{257–264}$ CD8$^+$ T cell epitope (HSV$_{TOM-OVA}$). When C57BL/6 mice were locally infected in the skin with either recombinant HSV-1 strain, multiple small foci composed of dozens of infected keratinocytes could be detected in the skin by immunohistochemistry and intravital imaging within 24 h postinfection (Fig. 1A, 1B). Consistent with prior data (16), infected microlesions were confined to the epidermal layer (Fig. 1A). Over a period of 3–4 d, these HSV-induced lesions fused together to form vesicles (Supplemental Fig. 1A) that were also noticeable by visual inspection (Fig. 1C).

Control of HSV-1 infection depends on T cell immunity, as shown by the fact that infection of T cell–deficient mice is lethal (20). To determine whether CD8$^+$ T cells also have a role in the control of infection in our recombinant HSV model, we transferred
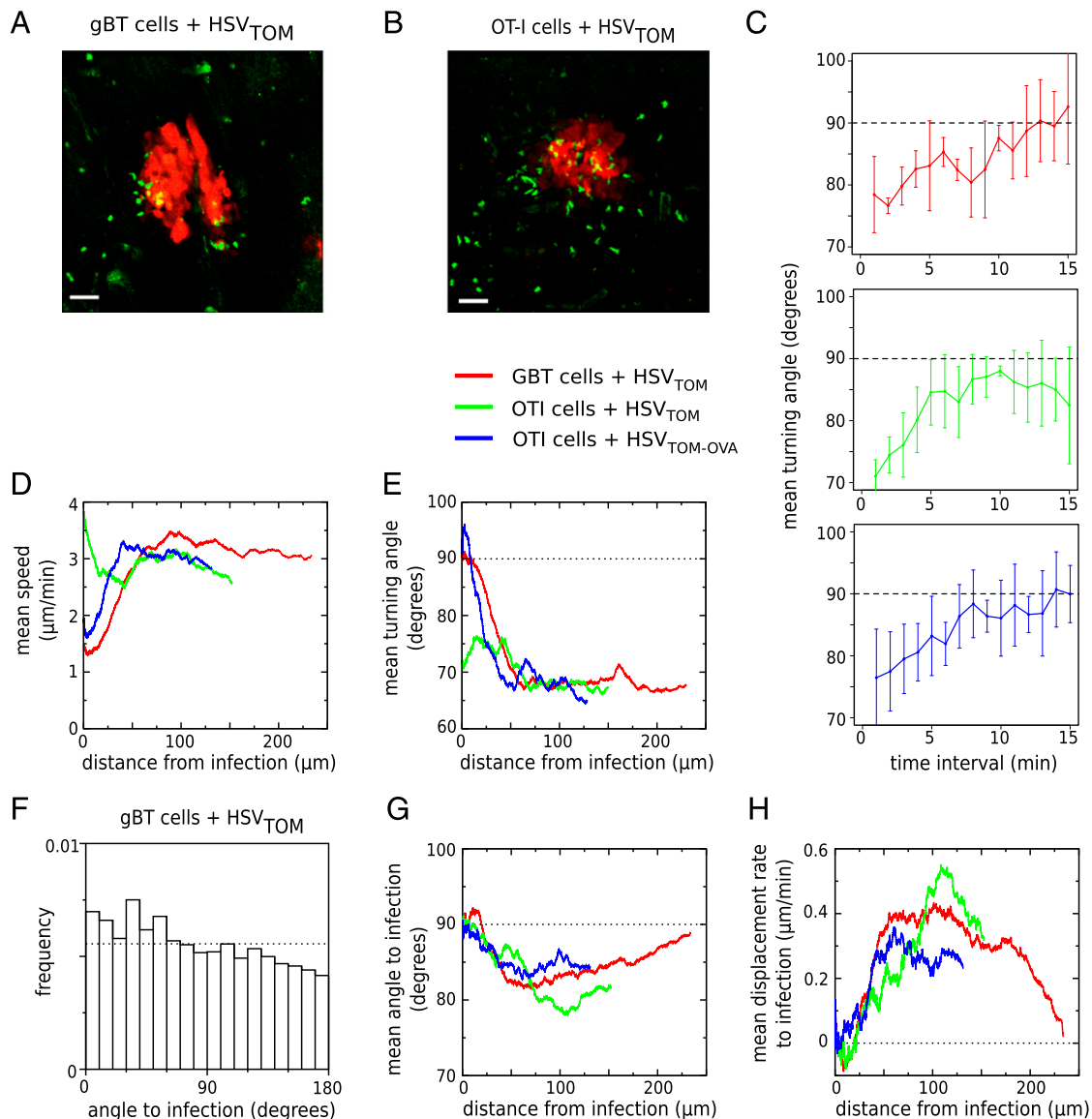
FIGURE 2. CTLs migrate preferentially toward infected microlesions. (**A** and **B**) Still confocal images of effector T cells (green) and HSV-1–infected microlesions (red) in epidermal skin of recipients of GFP-gBT (A) and GFP-OTI (B) CD8$^+$ T cells. Scale bar, 50 µm. (**C**) Turning angle (mean ± SD over the different videos) as a function of the time interval of measurement. The leveling off for large time intervals represents a measure of the persistence time of migration. (**D** and **E**) Mean speed (D) and mean turning angle between one-minute measurement intervals (E) of skin-infiltrating effector T cells are depicted as a function of the mean distance to the border of the infection. (**F**) Distribution of angles to infection for GFP-gBT T cells for all tracked migration steps. (**G** and **H**) Mean angle to infection (G) and mean displacement rate toward infection (H) of skin-infiltrating effector T cells are depicted as a function of the mean distance to the border of the infection. In (D), (E), (G), and (H), all tracked movement steps were sorted according to distance from infection (after merging data from multiple experiments), and a running average of 2000 data points was plotted (note that for each "bin" the mean value is calculated for both axes). Colors represent the following groups: GFP-gBT T cells (four videos from four mice; red), GFP-OTI T cells in animals infected with HSV$_{TOM}$, (five videos from five mice; green), and GFP-OTI T cells in animals infected with HSV$_{TOM-OVA}$ (four videos from four mice; blue).

GFP-transgenic gBT I.1 TCR transgenic T cells and boosted their numbers by vaccination before infection with HSV$_{TOM}$ (Supplemental Fig. 1B, 1C). Importantly, skin viral titers in HSV$_{TOM}$-infected mice harboring vaccine-activated GFP-gBT cells were markedly reduced ($p < 0.001$ relative to controls; Fig. 1D). T cell control of epithelial HSV infection was also apparent by macroscopic appearance (Fig. 1C).

Analysis of viral titers at different time points postinfection demonstrated that HSV-1 specific effector T cells displayed the most pronounced effect on HSV infection between 24 and 48 h of virus exposure (Fig. 1D), and subsequent imaging was performed at 24 h postinfection, before the occurrence of blisters and scabs that impede intravital imaging.

Imaging of HSV$_{TOM}$-infected skin demonstrated that effector T cell infiltration occurred for both HSV-specific and bystander (OTI) T cells (Fig. 2A, 2B; Supplemental Videos 1–3). To subsequently visualize the movement of effector T cells within the epidermis, infected skin areas infiltrated with GFP$^+$CD8$^+$ T cells were imaged at 1-min intervals for up to 1 h (without any measurable phototoxicity, as measured by speed over time; Supplemental Fig. 2). Whereas both gBT and OTI T cells actively moved around HSV$_{TOM}$-infected microlesions with a persistence time of 5–10 min (Supplemental Videos 1–3; Fig. 2C), only gBT cells arrested in close proximity to sites of infection, as demonstrated by decreased speed and loss of persistent migration when comparing steps close to (0–25 µm) and
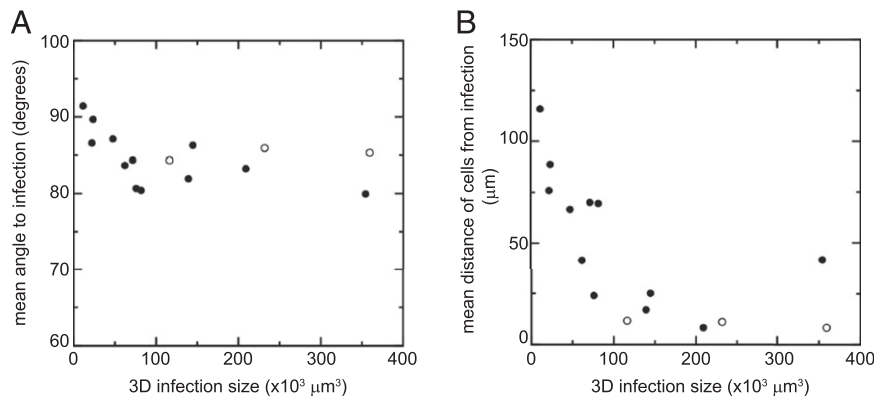
FIGURE 3. Correlation of HSV-1–infected microlesion size and T cell attraction and spatial distribution. (**A**) Attraction strength and (**B**) and spatial distribution of effector T cells are plotted as a function of the measured 3D microlesion size at the start of each experiment (data from 15 imaging regions in total). To allow for a fair comparison between experiments, distance data >200 μm from infection were discarded for all experiments (open circles indicate videos for which the most remote data point was <200 μm from infection, and closed circles indicate experiments for which the most remote data point was at least 200 μm from infection). As a measure of attraction strength, we first calculated the mean 2D angle to infection per distance-to-infection bin of size 20 μm, and subsequently calculated the mean of all 10 bins (0–200 μm distance from infection) for each video. This was done to prevent a large interexperimental variation in the fraction of data points close to and far away from the infection that would affect the results (e.g., a strong chemoattraction by a lesion could be obscured by the fact that many cells already arrived at the infection, due to the very same attraction). As a measure of spatial distribution of cells, the median distance from infection of all cells present at the first time point of imaging (i.e., at 24 h postinfection) was calculated.

far from (>25 μm) the infection (Fig. 2D, 2E; gBT + HSV$_{TOM}$: $p = 0.000$ [speed close versus far]; $p = 0.000$ [turning angles close versus far]; Mann–Whitney U test; 3D analysis in Supplemental Fig. 3A, 3B). This T cell arrest was due to Ag recognition (24), as OTI T cells in the skin of mice infected with HSV$_{TOM-OVA}$ also decreased their speeds close to the site of infection (OTI + HSV$_{TOM-OVA}$: $p = 0.000$ [speed close versus far]; $p = 0.000$ [turning angles close versus far]; Mann–Whitney U test), whereas OTI bystander T cells even slightly sped up close to HSV$_{TOM}$ infections (OTI + HSV$_{TOM}$: $p = 0.002$ [speed close versus far] and $p = 0.64$ [turning angles close versus far]; Mann–Whitney U test). Note that Ag-specific T cell arrest took place at up to a few dozen micrometers away from the estimated infection border, suggesting that T cells can detect Ag expressed by newly infected cells before the fluorescent signal becomes apparent.

Subtle directed migration of skin effector CD8$^+$ t cells

To determine by which migration strategy effector T cells reach foci of infection after tissue entry, we quantified the angle to infection (i.e., the angle between the measured travel direction and the shortest route toward the infection) for each movement step. The distribution of all the measured angles to infection was close to a uniform distribution (Fig. 2F). However, despite this highly erratic migration of T cells, there was a small bias toward acute angles (<90 degrees), suggesting that T cells had a small preference to migrate toward the infection. To study whether this effect was dependent on the distance from infection, average angles to infection were plotted as a function of distance to the infection (23). At the vicinity of the infection (0–25 μm), angles to infection were not significantly different from 90 degrees (Fig. 2G; gBT + HSV$_{TOM}$: $p = 0.51$; OTI + HSV$_{TOM}$: $p = 0.32$; OTI + HSV$_{TOM-OVA}$: $p = 0.59$; Mann–Whitney U test; 3D analysis in Supplemental Fig. 3C), implying random migration. In contrast, migration angles of T cells located further away from the infection ($>25\mu$m) were significantly smaller than 90 degrees (gBT + HSV$_{TOM}$: $p = 0.003$; OTI + HSV$_{TOM}$: $p < 0.001$; OTI + HSV$_{TOM-OVA}$: $p = 0.003$; Mann–Whitney U test). Thus, while T cells around HSV-infected lesions do migrate in all directions, a small but highly significant preference for directions that bring the cell closer to the site of infection is observed. Note that the angular preference at different distances is not a precise, fixed cellular be-

havior. Rather, the highly erratic migration that is superimposed over the preferential migration (Fig. 2F) gives rise to fluctuations even when many measurements are averaged as in Fig. 2G. The distance-dependent preferential migration was similar for Ag-specific and bystander T cells (Fig. 2G and Supplemental Fig. 3C; differences between mean angles to infection were nonsignificant for all comparisons; Mann–Whitney U test). Thus, the attracting component in T cell migration is independent of cognate Ag. Finally, when T cell migration was analyzed as the average displacement rate of cells toward the infection as a function of distance from infection (Fig. 2H; 3D analysis in Supplemental Fig. 3D), a distance-dependent pattern of attraction toward the site of infection was observed for all three conditions tested. Specifically, whereas close to the infection (up to 25 μm away) displacement rates toward infection were not different from 0 μm/min (gBT + HSV$_{TOM}$: $p = 0.60$; OTI + HSV$_{TOM}$: $p = 0.42$; OTI + HSV$_{TOM-OVA}$: $p = 0.57$; Mann–Whitney U test), further away from the infection (>25 μm away) an average displacement rate of 0.3–0.4 μm/min— significantly different from zero (gBT + HSV$_{TOM}$: $p = 0.002$; OTI + HSV$_{TOM}$: $p < 0.001$; OTI + HSV$_{TOM-OVA}$: $p = 0.027$; Mann–Whitney U test)—was observed. In summary, effector T cells in the epidermis migrate in all directions, but with a small, Ag-independent preference for movement toward infected areas.

Influence of infection size on attraction and spatial distribution of effector T cells. From our cell migration analysis, it is apparent that the strength of attraction (the deviation in angles to infection from 90 degrees) varies between experiments. We considered the possibility that the size of HSV foci may affect the strength of the chemoattractant gradient, such that larger foci of infection may attract CTLs more strongly. We therefore quantified the size of the infection at the beginning of each experiment and measured the strength of directed migration, by calculating the mean of angles to infection up to a distance of 200 μm. The relationship between these two measures shows that effector CD8$^+$ T cells are more strongly attracted toward large than toward small microlesions (Fig. 3A), although there appears to be a saturation effect for large infections.

Since microlesion size influences attraction strength (Fig. 3A), and attraction strength influences effector T cell arrival at microlesions, we predicted that for large foci of infection a larger
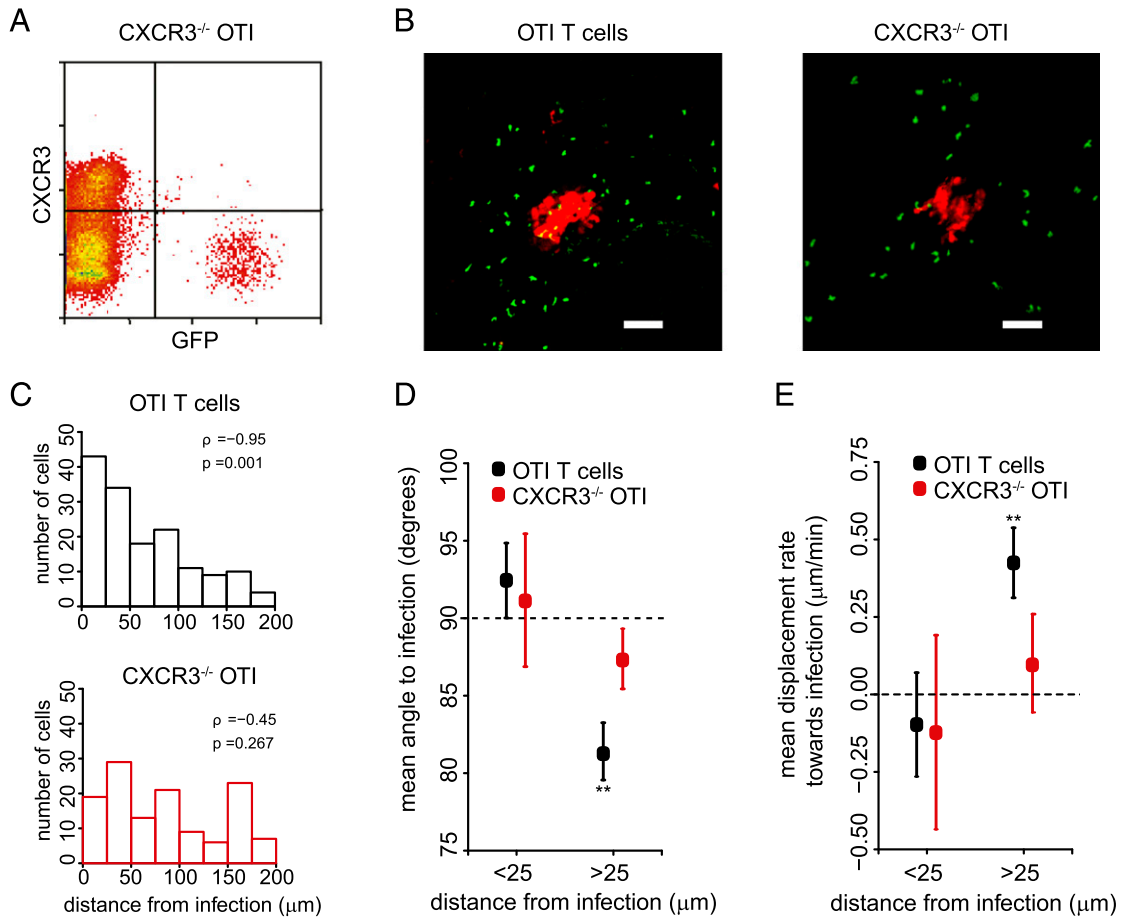
FIGURE 4. Directed migration of CTLs is CXCR3 dependent. (**A**) Recipients of naive GFP-OTI-CXCR3$^{-/-}$ T cells were vaccinated with DNA encoding the SIINFEKL epitope to activate the adoptively transferred cells. (**B**) Still confocal images of GFP-OTI or GFP-OTI-CXCR3$^{-/-}$ T cells (green) and HSV$_{TOM}$ microlesions (red) in epidermal skin. Scale bar, 100μm. (**C**) Comparison of the experimental spatial distributions of GFP-OTI or GFP-OTI-CXCR3$^{-/-}$ T cells (pooled from five imaging regions from five and two mice, respectively) at 24 h post HSV$_{TOM}$ infection. (**D**) Mean angle to infection and (**E**) displacement rate toward infection for GFP-OTI or GFP-OTI-CXCR3$^{-/-}$ T cells close (<25 μm) or far (>25 μm) from the infection. Wild type OTI T cells far away from the infection displayed migration parameters that differed significantly from the values expected for random migration (denoted by dashed lines). The migration pattern of GFP-OTI-CXCR3$^{-/-}$ T cells is, on the contrary, consistent with random migration. ** $p < 0.005$.

fraction of CTLs should be located close to the microlesion than for small foci. We quantified the spatial distribution of effector T cells at the beginning of each experiment by calculating the median of their distances to the infection. As predicted, for large foci, CTLs were located at shorter median distances than for small infections (Fig. 3B). These data indicate that the volume of the infected microlesion correlates with the strength of effector T cell attraction, and—presumably because of this —the spatial distribution of these cells around the lesion. Note that these data are also consistent with a scenario in which T cells arriving early at
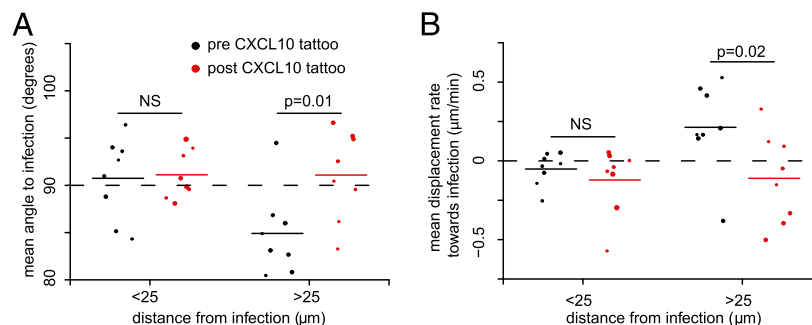
FIGURE 5. Directed migration of effector T cells is lost upon disturbance of chemokine gradient. (**A** and **B**) OTI T cells migrating toward an infected microlesion were imaged before or after local CXCL10 microinjection (to disrupt the chemotactic gradient). Movement steps were binned according to their distance to the infection, and the mean angle to infection (A) and mean displacement rate toward infection (B) of all steps within the bin was calculated (i.e., each infection focus is represented by two dots, one in each distance bin). The size of each dot is representative of the number of movement steps on which the average is based, using a "relative" log scale (e.g., a doubling of the radius of a circle implies a 10-fold increase in the number of data points). The "post CXCL10 tattoo" analysis is based on eight infection foci from three mice, and the "pre CXCL10 tattoo" on eight foci from seven mice (combining the five foci from Fig. 2 with three newly imaged foci).
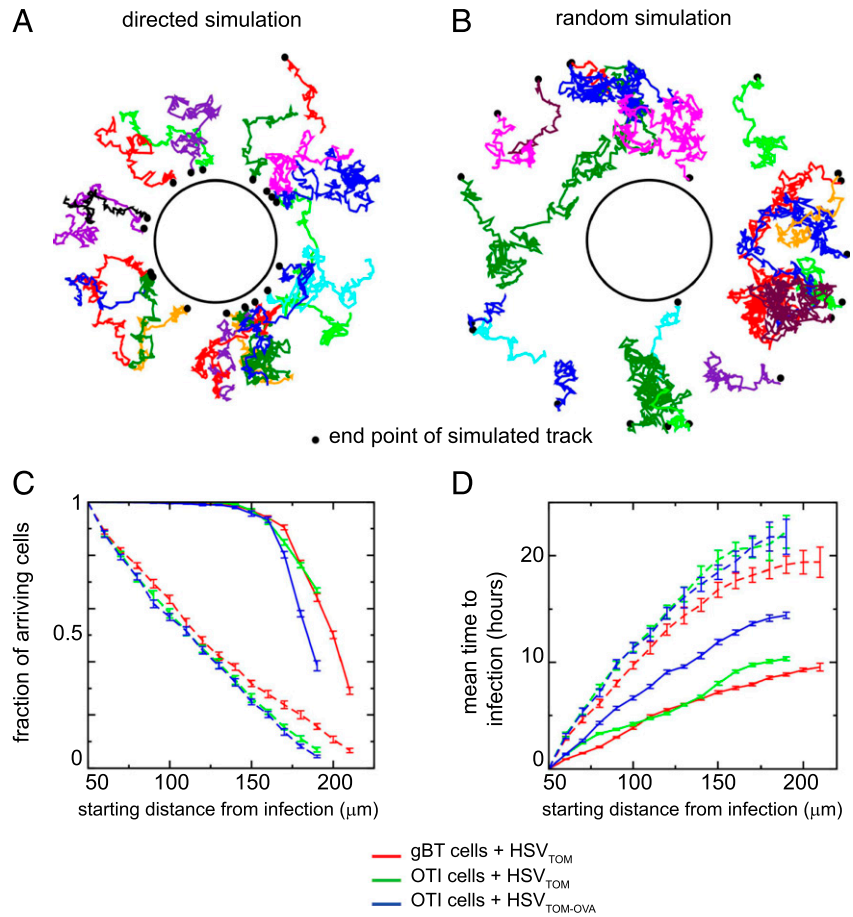
FIGURE 6. Simulating the effect of directional migration on T cell arrival. (**A** and **B**) Example of tracks of 20 in silico gBT T cells starting 150 μm from an infection with radius $r = 100$ μm, constructed by "directed" (A) or "random" (B) 2D simulations. The black circle indicates the perimeter of the simulated infection, and the black dots represent the final positions of cells. (**C** and **D**) The fraction of cells arriving 50 μm from an infection with radius $r = 100$μm (C) and the mean time to achieve this (D), when starting from various distances to infection in 2D simulations. For each starting distance to infection, 20 simulations of 1000 cells were performed; mean and SD of the simulations are plotted. Results from directed simulations are shown as solid lines, and results from random simulations are shown as dashed lines. Simulations are based on cell migration data from GFP-gBT T cells and GFP-OTI T cells in animals infected with HSV_{TOM} (red and green, respectively), and of GFP-OTI T cells in animals infected with $HSV_{TOM-OVA}$ (blue). Migration data from gBT cells at distances to infection greater than ~210 μm were omitted from the analysis to allow for a fair comparison between experimental conditions.

infection foci secrete chemokines upon target encounter, thereby reinforcing the attraction of yet more effector T cells (in a similar fashion, specific $CD8^+$ T cells clustering around malaria-infected hepatocytes were proposed to locally secrete factors that result in the recruitment of additional effector T cells (15).

Because the size of the infection affects the behavior of surrounding T cells, only infections with a minimum volume of 50,000 μm^3 (as estimated from the image voxels assigned to infected cells) were included. Note that small infections below this threshold were primarily observed for $HSV_{TOM-OVA}$, suggesting that this modified virus grows out less efficiently than HSV_{TOM}.

CXCR3 mediates chemotaxis of effector T cells in the skin

Based on recent data by Hickman et al. (7) in VV infection, the chemokine receptor CXCR3 is the primary candidate for mediating the subtle chemotaxis that we detected from the cell migration analysis. To test whether CXCR3 and its ligands are indeed responsible for chemotaxis, we transferred GFP-OTI-CXCR3$^{-/-}$ cells (CXCR3$^{-/-}$ cells; Fig. 4A) into C57BL/6 mice, which were then vaccinated with SIINFEKL and infected with HSV_{TOM}. After HSV_{TOM} administration, effector T cells from CXCR3$^{-/-}$ donor origin were found at the site of infection, albeit at slightly lower frequencies than wild type cells were. Consistent with the results by Hickman et al. (7) for VV infection, this result suggests that CXCR3 expression is generally dispensable for T cell activation and tissue extravasation. For wild type OTI T cells infiltrating the area of infection, a strong accumulation around sites of infection and a consistent decline of T cell numbers with increasing distances of infection are expected, whereas an approximately flat spatial distribution would be expected for CXCR3$^{-/-}$ T cells if signaling through this receptor is responsible for the observed directional

migration. In line with this expectation, there was a significant negative correlation ($p = 0.001$) between T cell numbers and distance from infection for wild type OTI T cells, and a nonsignificant correlation for CXCR3$^{-/-}$ OTI T cells (Fig.4B, 4C). Furthermore, whereas control T cells showed directed migration at long distances from the infection, no significant directed migration could be detected for CXCR3-deficient T cells (Fig. 4D, 4E). The small (nonsignificant) directed migration component that might still be present could suggest that other chemokine receptors also have a limited role in attracting T cells toward infection foci. However, signaling via CXCR3 clearly explains the bulk of the directional migration observed.

As an independent test for the involvement of CXCR3 that does not rely on genetic deficiency of the receptor, we explored the effect of local delivery of CXCL10. When the pre-existing chemokine gradient was disrupted by local delivery of CXCL10 by tattoo application into an area that was larger than that in which the T cells were localized, the consistent pattern of T cell migration toward foci of infection was no longer observed. Specifically, T cells around individual foci revealed either migration away from or toward foci or migration in an approximately random pattern, consistent with the notion that T cells were attracted to newly created CXCL10 hotspots (Fig. 5). Collectively, these data show that the directed migration displayed by CTLs in proximity of foci of infection is largely mediated by CXCR3 and its ligands.

Modeling the consequence of directed migration of effector T cells

The observed directional preference of CTLs toward sites of infection is relatively small (Fig. 2G, 2H; Supplemental Fig. 3), and the variation among all measured angles to infection is large (Fig.
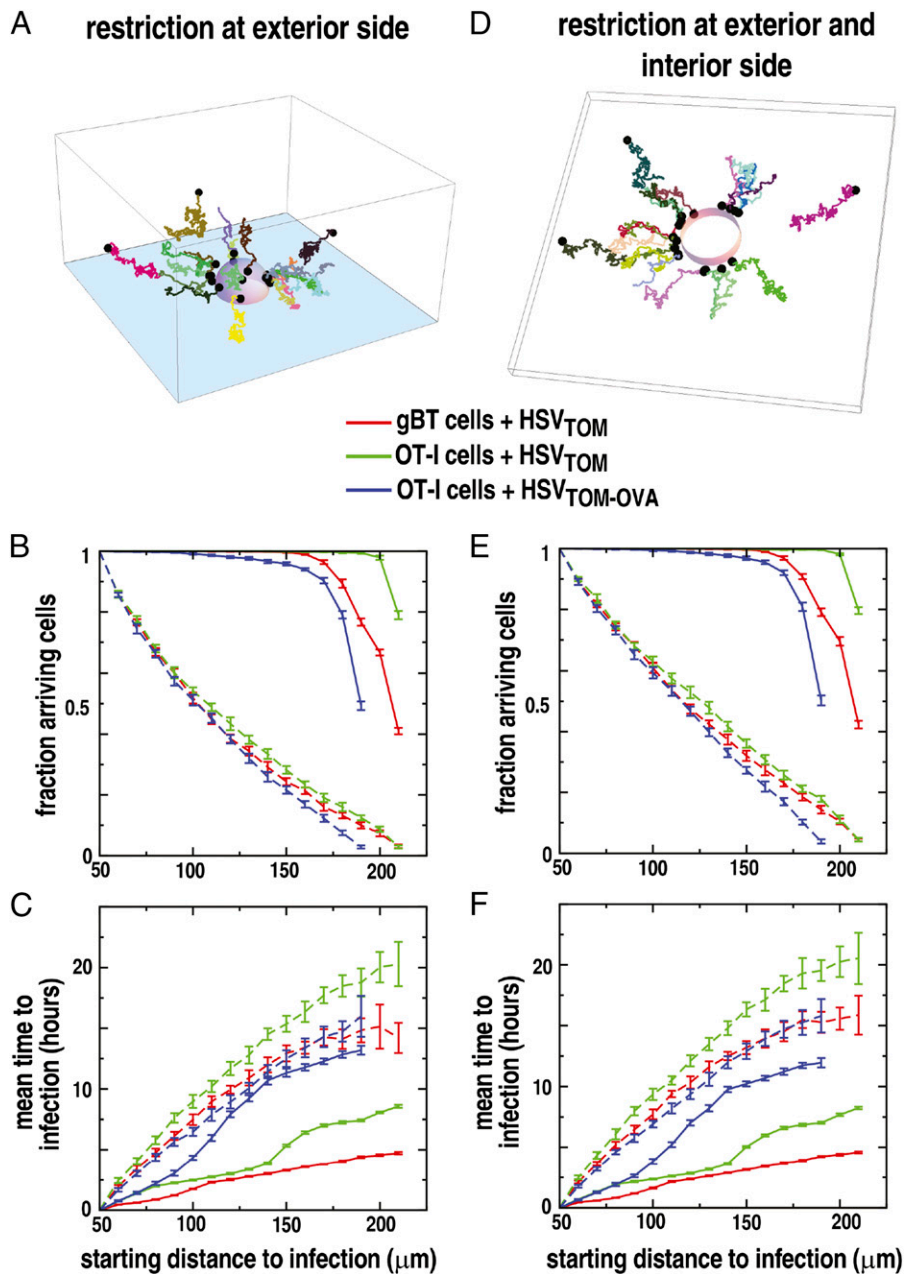
FIGURE 7. 3D simulations demonstrate effective and fast arrival of effector T cells at target site. (**A** and **D**) Example of tracks of 20 in silico gBT T cells starting 150 μm from an infection with radius $r = 100$ μm, constructed by 3D simulations with restriction at the exterior side (A) or at both the exterior and interior sides (D). The purple-colored hemisphere, or ring, represents the simulated infection; dots represent the final position of the simulated cells. (**B**, **C**, **E**, and **F**) The fraction of cells arriving 50 μm from an infection with radius $r = 100$ μm (B and E) and the mean time to achieve that position (C and F), when starting from various distances from the infection in 3D simulations. For each starting distance from infection, 20 simulations of 1000 cells were performed, and mean and SD of the simulations are plotted. Results from directed simulations are depicted with solid lines, and results from random simulations are depicted with dashed lines. Simulations are based on cell migration data from GFP-gBT T cells (red) and GFP-OTI T cells in animals infected with HSV_{TOM}, (green), and from GFP-OTI T cells in animals infected with $HSV_{TOM-OVA}$ (blue). Migration data from gBT T cells at distances to infection greater than ~210 μm were discarded to allow for a fair comparison between experimental conditions. The results of the 3D simulations are in accordance with those of the 2D simulations (Fig. 3), and they demonstrate that the measured directional preference has a major effect on the kinetics and effectiveness of T cell arrival close to the infection.

2F; Supplemental Fig. 4, *lower panels*), thereby explaining why directional migration is not apparent from visual inspection of in vivo imaging data (Supplemental Videos 1–3). To determine to what extent T cell arrival at sites of infection is influenced by this small directional preference, we generated realistic, long-lasting tracks based on experimental data, using a computational approach similar to that in previously published work (10, 25, 26). We reconstructed cellular migration paths using the experimentally measured distributions of speed, angle to infection, and turning angle. Furthermore, because the distance to infection at which cells are located determines the typical values found for these three parameters, we chose combinations of speed and migration angles from data points that were binned with respect to their distance from the infection. Note that we did not explicitly incorporate full cellular arrest because of synapse formation with target cells in the simulations, but the in silico cells drastically slow down close to the infection (i.e., for HSV-specific T cells, see Fig. 2D).

During each simulation, *in silico* CTLs started at a predefined distance away from the circular (or spherical) infection, and combinations of speed and migration angles were drawn at random from the experimental distributions found around that distance. The resulting migration step determined the position, and therefore the distance to the infection, of the next time step. This procedure was repeated until a cell arrived in proximity of the infection (using a distance threshold of 50 μm) or left the space for which we had experimental data (i.e., reached distances too far away from the infection). The tracks generated (e.g., Fig. 6A) matched the experimental data closely in terms of their distributions of speed, angles to infection, and turning angles (Supplemental Fig. 4). In addition to these directed simulations, we also performed random simulations in which we substituted the experimentally found distribution of angles to infection with a random distribution, while keeping the persistence and speed of cells according to the experimental measurements (Fig. 6B).
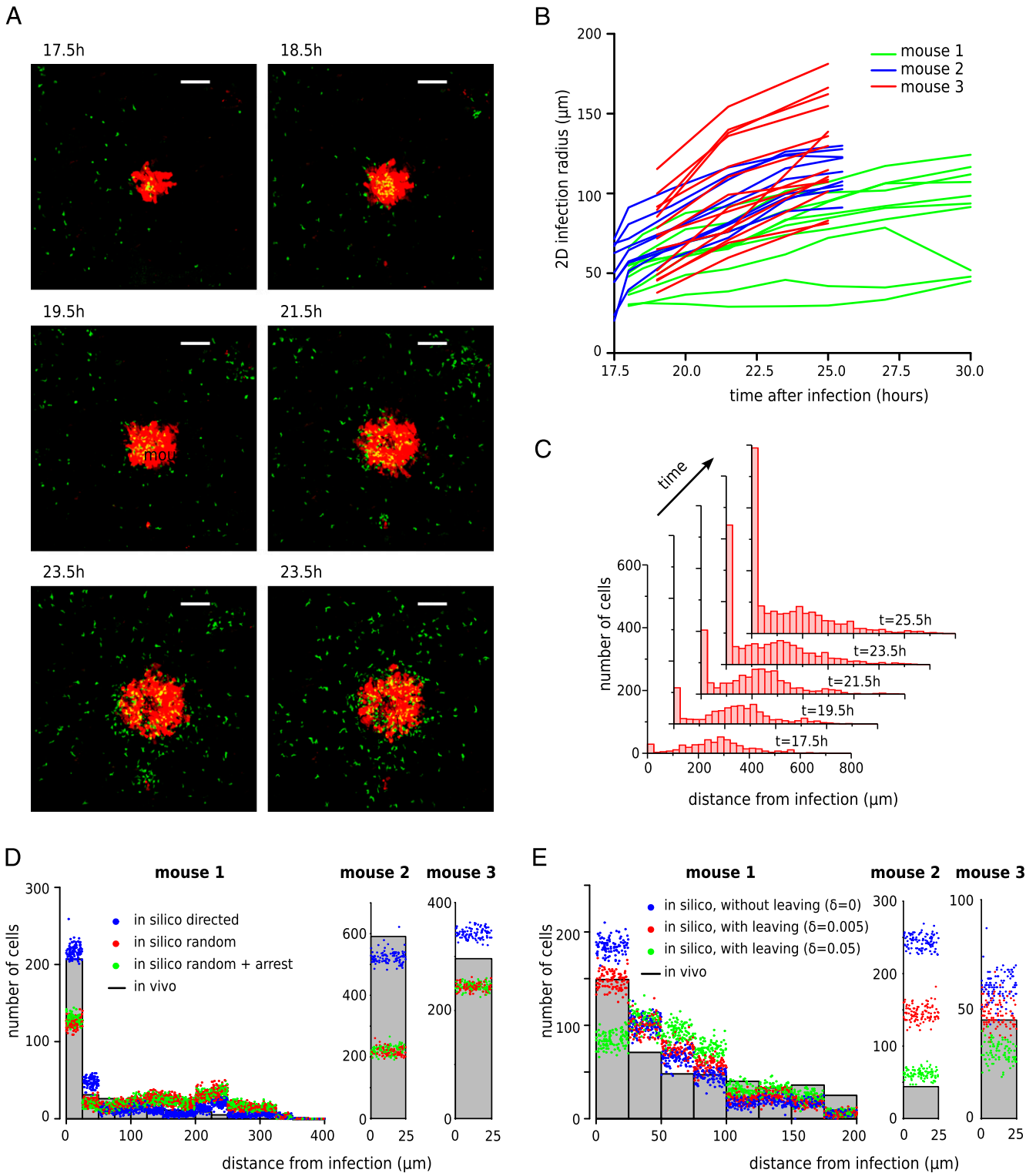
FIGURE 8. CTLs accumulate around infected microlesions over time. (**A**) Still confocal images of GFP-gBT T cells (green) and microlesions (red) in epidermal skin, showing accumulation of T cells close to the infection over time. Scale bar, 100 μm. (**B**) Evolution of infection growth over time for 31 different foci of three mice. Note that while our estimate of infection size is probably a slight underestimate, because fluorescence signal needs to accumulate to a sufficient level to allow detection, this is expected to be a constant effect and thereby unlikely to affect the estimate of the radial growth. (**C**) Evolution of the distance distribution of effector T cells over time. Data of consecutive image sequences obtained from eight different infected areas within a single mouse (representative of three mice) were combined. (**D**) Comparison of the experimental spatial distributions of gBT cells and the distributions of gBT cells from simulations in which migration was directed, random, or random with full arrest upon arrival, in the context of a growing infection. In silico cells were simulated considering a combination of 1) the initially observed spatial distribution taken from experimental data at ~17 h postinfection, 2) the entry of new cells in the epidermis at random time points and at random locations in the simulated space, 3) an initial infection radius as estimated from the images, and 4) a growth of the infection radius at a rate determined from the experimental images (~0.1 μm/min). Bars represent the experimental distribution at the last time point of imaging, and dots represent the simulated distributions. Note that the simulations exhibit a peak in cell number ~200 μm from infection; this is due to a transition to random migration and possible attraction toward a neighboring infection focus at (*Figure legend continues*)

Both specific and bystander cells starting at a distance of up to ~150 μm arrived with almost 100% efficiency close to the infection when directed simulations were performed (Fig. 6C). In contrast, for randomly moving cells, regardless of their specificity, the fraction of cells that reached the target was only ~30%. Furthermore, the cells that did arrive at the infection by random migration required approximately twice the amount of time as directional cells (Fig. 6D). The differences between directed and random simulations were observed when simulations were performed in 2D (Fig. 6) in one-side-restricted or two-side-restricted 3D (Fig. 7) simulations. In conclusion, our 2D and 3D simulations predict that the subtle chemotaxis of CTLs toward sites of infection are highly important for the rapid arrival of the majority of CTLs that are present in the tissue.

Long-term in vivo imaging confirms predicted CTL accumulation

In the above experiments, we used short-term imaging data to generate simulations that showed the long-term consequences of the observed bias in angles to infection (Figs. 6, 7). These simulations rely on two essential assumptions: first, that the T cell migration parameters observed during imaging at 24 h postinfection hold true for longer periods, and second, that the T cell migration parameters measured are the major factors in driving T cell accumulation, rather than T cell division, death, or exit. To test whether in vivo T cell accumulation followed the pattern predicted by our simulations, we performed long-term–long-interval in vivo imaging experiments (lasting up to 12 h), monitoring both the spatial distribution of gBT T cells and infection growth (Fig. 8A–C). Analysis of the still images showed a clear accumulation of T cells close to the infection over time (Fig. 8A).

We then simulated CTL migration toward the infection, using the distance distribution observed at the first still time point of imaging (~17 h) as a starting distribution; in addition, we simulated new cells entering the simulated field at a random position in space and time, such that the same amount of cells was present at the final time point in our simulations as in the imaging data set. Finally, we took into account the infection growth observed during imaging. The spatial distributions at the end of the directed simulations (up to 12 h) matched the experimentally observed spatial distributions well (Fig. 8D, blue dots). In contrast, the match between the spatial distribution observed in random simulations and that observed in vivo was poor (Fig. 8D, red dots), even in a variant of these simulations in which we incorporated full arrest when cells reached the simulated infection (Fig.8D, green dots). Finally, the low level of accumulation observed in random simulations is mainly caused by cellular entry into the epidermis close to the infection, rather than by intraepidermal migration followed by arrest. On the basis of these data, we conclude that the accumulation observed in vivo requires directional migration, and it cannot be explained by random migration combined with arrest close to the infection.

To explore the same issue for T cells that do not encounter cognate Ag, we subsequently performed the same imaging and simulation procedure for OTI bystander cells, which continue migrating when entering the lesion. In this case, directed migration alone consistently overpredicted the accumulation of effector cells

close to the infection (Fig. 8E). Extension of the simulations with a probability to leave the infiltrated area after arrival at the infected site (e.g., by exit of the imaging field toward the dermis) improved the correspondence between predicted and observed spatial distribution. This result suggests that T cells that fail to detect cognate Ag may have an increased probability to leave the infiltrated area after a period of unfruitful search. Direct quantification of such bystander leaving during dynamic imaging is precluded in our setup because the thin image volume leads to many fake entry and exit events, which would strongly dominate true events.

Discussion

The main finding of the current study is that effector CD8^{+} T cells in skin epithelium approach clusters of infected cells by subtle chemotaxis. This directed migration can be described as a small preference for movements toward the microlesion in an otherwise highly irregular trajectory, and in fact the T cells move away from the sites of infection almost as often as they move toward it.

The observed CXCR3-mediated attraction of T cells by clusters of infected cells implies the existence of a chemoattractant gradient, and the finding that the strength of T cell attraction correlates with lesion size is also consistent with this notion. If T cells are guided to sites of infection by a gradient, why is their migration pattern so erratic? One explanation is that T cell migration has to occur through a bed of tightly linked keratinocytes, thereby severely limiting the number of potential trajectories. This, however, does not seem to explain why T cells also frequently move away from the site of infection. Conceivably, the gradient that is sensed by the cells is locally stochastic and shallow. A shallow chemotactic gradient can make it difficult for small cells such as T lymphocytes to respond to the signal because of the minimal difference in signal strength sensed by the front and back end of the cell (27). However, neutrophils have a similar size as T cells and seem to be able to migrate directionally in a much more pronounced manner, both intravascularly and within peripheral tissues (28–30). Thus, it might also be a general property of T cells that random and persistent trajectories are adjusted only slightly upon encountering chemoattractant gradients, possibly to allow the scanning of a larger area of the peripheral tissue.

Upon HSV infection, both specific and bystander effector T cells are found within the infected area (Fig. 2A), consistent with prior data from other groups regarding the behavior of effector T cells in tumors and infected tissues (7, 24, 31, 32). The presence of substantial numbers of nonspecific T cells could reduce the efficiency of cognate CTL-target cell contacts by steric hindrance. For the similar case of T cell scanning of dendritic cells within lymph nodes, we recently demonstrated that such competition can be alleviated if bystander T cells lose their sensitivity to chemokine upon reaching the APC (33). By the same token, in the case of skin infection, this 'logistic' problem could be reduced when effector T cells that do not encounter their cognate Ag were to leave the infected area, a concept that is supported by our in silico simulations of bystander cells.

Two observations suggest that the chemoattraction we describe here is biologically meaningful. First, the pattern of T cell accumulation that is measured experimentally is reproduced in computer simulations in which the observed directional migration is

great distances, which in the simulation leads to cells lingering at distances of ~200 μm. (**E**) Comparison of the experimental spatial distributions of OTI cells surrounding a HSV_TOM microlesion (based on 17 imaging regions from 3 mice) and the distributions of OTI cells from 2D simulations in which migration was either "directed without leaving" or "directed with leaving" in the context of a growing infection. In directed simulations with leaving, T cells that reached the infection earlier during the simulation left with probability δ at each time step. In (D) and (E), the complete experimental and simulated spatial distributions are shown for one mouse; for two more mice, only the bin closest to the infection is shown.

incorporated, but not in simulations in which accumulation is driven by a combination of random T cell migration and T cell arrest close to the infection. Second, the observed chemotaxis influences T cell arrival on a time scale that is relevant to the kinetics of HSV-1 spreading within the infected skin (according to our in vivo measurements by a radial growth of approximately three cell layers, in 5 h). To our knowledge, this study presents the first direct evidence of chemoattraction toward regions of interest of effector T cells within a peripheral tissue. Prior studies in other peripheral tissues did not detect directional migration (16, 17), or postulated its occurrence on the basis of indirect observations (7, 15). It may be interesting to reanalyze such existing data by the strategies used here, to evaluate whether similar subtle migration behaviors are hidden in time-lapse imaging data sets.

Acknowledgments

Disclosures

References

1. Alvarez, D., E. H. Vollmann, and U. H. von Andrian. 2008. Mechanisms and consequences of dendritic cell migration. *Immunity* 29: 325–342.
2. Heath, W. R., and F. R. Carbone. 2009. Dendritic cell subsets in primary and secondary T cell responses at body surfaces. *Nat. Immunol.* 10: 1237–1244.
3. Rose, D. M., R. Alon, and M. H. Ginsberg. 2007. Integrin modulation and signaling in leukocyte adhesion and migration. *Immunol. Rev.* 218: 126–134.
4. Filipe-Santos, O., P. Pescher, B. Breart, C. Lippuner, T. Aebischer, N. Glaichenhaus, G. F. Späth, and P. Bousso. 2009. A dynamic map of antigen recognition by CD4 T cells at the site of *Leishmania major* infection. *Cell Host Microbe* 6: 23–33.
5. Schaeffer, M., S. J. Han, T. Chtanova, G. G. van Dooren, P. Herzmark, Y. Chen, B. Roysam, B. Striepen, and E. A. Robey. 2009. Dynamic imaging of T cell-parasite interactions in the brains of mice chronically infected with *Toxoplasma gondii*. *J. Immunol.* 182: 6379–6393.
6. Wilson, E. H., T. H. Harris, P. Mrass, B. John, E. D. Tait, G. F. Wu, M. Pepper, E. J. Wherry, F. Dzierzinski, D. Roos, et al. 2009. Behavior of parasite-specific effector CD8+ T cells in the brain and visualization of a kinesis-associated system of reticular fibers. *Immunity* 30: 300–311.
7. Hickman, H. D., G. V. Reynoso, B. F. Ngudiankama, S. S. Cush, J. Gibbs, J. R. Bennink, and J. W. Yewdell. 2015. CXCR3 chemokine receptor enables local CD8(+) T cell migration for the destruction of virus-infected cells. *Immunity* 42: 524–537.
8. Worbs, T., T. R. Mempel, J. Bölter, U. H. von Andrian, and R. Förster. 2007. CCR7 ligands stimulate the intranodal motility of T lymphocytes in vivo. *J. Exp. Med.* 204: 489–495.
9. Germain, R. N., E. A. Robey, and M. D. Cahalan. 2012. A decade of imaging cellular motility and interaction dynamics in the immune system. *Science* 336: 1676–1681.
10. Beltman, J. B., C. D. C. Allen, J. G. Cyster, and R. J. de Boer. 2011. B cells within germinal centers migrate preferentially from dark to light zone. *Proc. Natl. Acad. Sci. USA* 108: 8755–8760.
11. Castellino, F., A. Y. Huang, G. Altan-Bonnet, S. Stoll, C. Scheinecker, and R. N. Germain. 2006. Chemokines enhance immunity by guiding naive CD8+ T cells to sites of CD4+ T cell-dendritic cell interaction. *Nature* 440: 890–895.
12. Hugues, S., A. Scholer, A. Boissonnas, A. Nussbaum, C. Combadière, S. Amigorena, and L. Fetler. 2007. Dynamic imaging of chemokine-dependent CD8+ T cell help for CD8+ T cell responses. *Nat. Immunol.* 8: 921–930.
13. Okada, T., M. J. Miller, I. Parker, M. F. Krummel, M. Neighbors, S. B. Hartley, A. O'Garra, M. D. Cahalan, and J. G. Cyster. 2005. Antigen-engaged B cells undergo chemotaxis toward the T zone and form motile conjugates with helper T cells. *PLoS Biol.* 3: e150.
14. Semmling, V., V. Lukacs-Kornek, C. A. Thaiss, T. Quast, K. Hochheiser, U. Panzer, J. Rossjohn, P. Perlmutter, J. Cao, D. I. Godfrey, et al. 2010. Alternative cross-priming through CCL17-CCR4-mediated attraction of CTLs toward NKT cell-licensed DCs. *Nat. Immunol.* 11: 313–320.
15. Cockburn, I. A., R. Amino, R. K. Kelemen, S. C. Kuo, S. W. Tse, A. Radtke, L. Mac-Daniel, V. V. Ganusov, F. Zavala, and R. Ménard. 2013. In vivo imaging of CD8+ T cell-mediated elimination of malaria liver stages. *Proc. Natl. Acad. Sci. USA* 110: 9090–9095.
16. Coppieters, K., N. Amirian, and M. von Herrath. 2012. Intravital imaging of CTLs killing islet cells in diabetic mice. *J. Clin. Invest.* 122: 119–131.
17. Harris, T. H., E. J. Banigan, D. A. Christian, C. Konradt, E. D. Tait Wojno, K. Norose, E. H. Wilson, B. John, W. Weninger, A. D. Luster, et al. 2012. Generalized Lévy walks and the role of chemokines in migration of effector CD8 + T cells. *Nature* 486: 545–548.
18. Mueller, S. N., W. Heath, J. D. McLain, F. R. Carbone, and C. M. Jones. 2002. Characterization of two TCR transgenic mouse lines specific for herpes simplex virus. *Immunol. Cell Biol.* 80: 156–163.
19. Toebes, M., M. Coccoris, A. Bins, B. Rodenko, R. Gomez, N. J. Nieuwkoop, W. van de Kasteele, G. F. Rimmelzwaan, J. B. Haanen, H. Ovaa, and T. N. Schumacher. 2006. Design and use of conditional MHC class I ligands. *Nat. Med.* 12: 246–251.
20. Halford, W. P., J. W. Balliet, and B. M. Gebhardt. 2004. Re-evaluating natural resistance to herpes simplex virus type 1. *J. Virol.* 78: 10086–10095.
21. Bins, A. D., A. Jorritsma, M. C. Wolkers, C. F. Hung, T. C. Wu, T. N. Schumacher, and J. B. Haanen. 2005. A rapid and potent DNA vaccination strategy defined by in vivo monitoring of antigen expression. *Nat. Med.* 11: 899–904.
22. Weeks, B. S., R. S. Ramchandran, J. J. Hopkins, and H. M. Friedman. 2000. Herpes simplex virus type-1 and -2 pathogenesis is restricted by the epidermal basement membrane. *Arch. Virol.* 145: 385–396.
23. Beltman, J. B., A. F. M. Marée, and R. J. de Boer. 2009. Analysing immune cell migration. *Nat. Rev. Immunol.* 9: 789–798.
24. Boissonnas, A., L. Fetler, I. S. Zeelenberg, S. Hugues, and S. Amigorena. 2007. In vivo imaging of cytotoxic T cell infiltration and elimination of a solid tumor. *J. Exp. Med.* 204: 345–356.
25. Beauchemin, C., N. M. Dixit, and A. S. Perelson. 2007. Characterizing T cell movement within lymph nodes in the absence of antigen. *J. Immunol.* 178: 5505–5512.
26. Figge, M. T., A. Garin, M. Gunzer, M. Kosco-Vilbois, K. M. Toellner, and M. Meyer-Hermann. 2008. Deriving a germinal center lymphocyte migration model from two-photon data. *J. Exp. Med.* 205: 3019–3029.
27. Bialek, W., and S. Setayeshgar. 2005. Physical limits to biochemical signaling. *Proc. Natl. Acad. Sci. USA* 102: 10040–10045.
28. McDonald, B., K. Pittman, G. B. Menezes, S. A. Hirota, I. Slaba, C. C. Waterhouse, P. L. Beck, D. A. Muruve, and P. Kubes. 2010. Intravascular danger signals guide neutrophils to sites of sterile inflammation. *Science* 330: 362–366.
29. Peters, N. C., J. G. Egen, N. Secundino, A. Debrabant, N. Kimblin, S. Kamhawi, P. Lawyer, M. P. Fay, R. N. Germain, and D. Sacks. 2008. In vivo imaging reveals an essential role for neutrophils in leishmaniasis transmitted by sand flies. *Science* 321: 970–974.
30. Lämmermann, T., P. V. Afonso, B. R. Angermann, J. M. Wang, W. Kastenmüller, C. A. Parent, and R. N. Germain. 2013. Neutrophil swarms require LTB4 and integrins at sites of cell death in vivo. *Nature* 498: 371–375.
31. Koya, R. C., S. Mok, B. Comin-Anduix, T. Chodon, C. G. Radu, M. I. Nishimura, O. N. Witte, and A. Ribas. 2010. Kinetic phases of distribution and tumor targeting by T cell receptor engineered lymphocytes inducing robust antitumor responses. *Proc. Natl. Acad. Sci. USA* 107: 14286–14291.
32. Mrass, P., H. Takano, L. G. Ng, S. Daxini, M. O. Lasaro, A. Iparraguirre, L. L. Cavanagh, U. H. von Andrian, H. C. Ertl, P. G. Haydon, and W. Weninger. 2006. Random migration precedes stable target cell interactions of tumor-infiltrating T cells. *J. Exp. Med.* 203: 2749–2761.
33. Vroomans, R. M. A., A. F. M. Marée, R. J. de Boer, and J. B. Beltman. 2012. Chemotactic migration of T cells towards dendritic cells promotes the detection of rare antigens. *PLOS Comput. Biol.* 8: e1002763.